Journal of Materials Chemistry A

Accepted Manuscript

ROYAL SOCIETY OF CHEMISTRY

www.rsc.org/materialsA

As consideration for the Table of Contents:

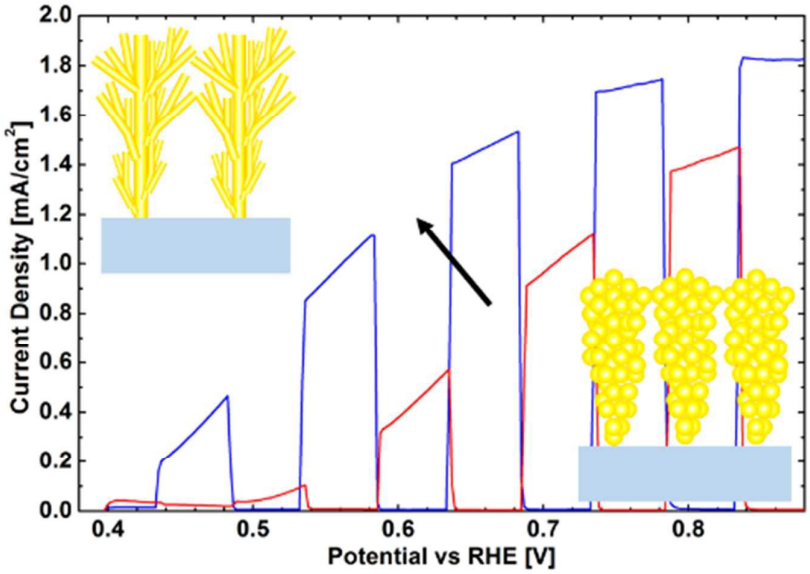

Journal Name

RSCPublishing

ARTICLE

Quasi-1D Hyperbranched WO_3 Nanostructures for Low Voltage Photoelectrochemical Water-Splitting

Cite this: DOI: 10.1039/xoxxoooooox

Received ooth January 2012,
Accepted ooth January 2012

DOI: 10.1039/xoxxoooooox

www.rsc.org/

Mehrdad Balandeh,[a,b,†] Alessandro Mezzetti,[a,c,†] Alessandra Tacca,[d] Silvia Leonardi,[a] Gianluigi Marra,[d] Giorgio Divitini,[e] Caterina Ducati,[e] Laura Meda,[d] Fabio Di Fonzo.[a,*]

Arrays of hyperbranched high aspect ratio mesostructures are grown by pulsed laser deposition, through a self-assembly process from the gas phase. These hierarchical arrays are used successfully as photoanodes for the photoelectrochemical splitting of water, exhibiting an onset potential as low as 0.4 V vs RHE and saturation current densities up to 1.85 mA/cm^2 at 0.8 V vs RHE. While the latter is similar to the state of the art values for WO_3 nanostructured photoanodes, both the onset and saturation voltages are significantly lower than any other report so far. This peculiar behavior is attributed to the hyperbranched structure and to its excellent optical and electronic properties.

With energy production through photovoltaics becoming a well-established technology, the next issue to address for a fully solar-based energetic economy is the need for an energy vector like standard fuels. The production of hydrogen via solar energy stands as one of the most promising answers to the problem, especially given the recent development in the field of hydrogen-based fuel cells. Photoelectrochemical (PEC) water-splitting provides a cheap and easy way to produce hydrogen from aqueous solutions using inexpensive and non-toxic metal oxide photoelectrodes. Increasing the photocurrent of the PEC devices through engineering of the working electrode has been the preferred way to enhance the solar-to-hydrogen efficiency of the water-splitting process. Another optimization strategy is to develop photoelectrodes that provide photocurrents at lower applied voltages, especially important in the field of PEC-PEC or PV-PEC tandem cell, where working points at low biases are of paramount importance. Pulsed laser deposition is employed to deposit tungsten oxide photoanodes, consisting of mesoporous hyperbranched nanostructures. These photoanodes display efficient charge generation - due to the improved light harvesting of the "tree-like" nanostructure - coupled with a low voltage photocurrent onset, thanks to the enhanced charge transport provided by the long range crystalline order of the hyperbranched morphology.

Introduction

Since Fujishima and Honda's discovery in 1972,[1] the research on materials capable of splitting water into its components and thus able to produce hydrogen through the use of solar radiation has greatly increased, leading to a rich literature of materials and morphologies capable of performing this task. Materials with suitable energy levels[2–5], both for absorption in the visible range and for correct energetic alignment with respect to the water electrolysis potentials, are being researched. This path includes experimenting with new materials, as well as modifying already known materials through doping[6–10] in order to change their inherent opto-electrical properties. Morphological modifications and nanostructuring[11–15] are employed to increase the photoelectrochemical performances of the devices, by improving the charge transport properties of the structures or enhancing the photogeneration of charges and thus the resulting photocurrent. Mesoporous materials[16–20] with high surface area and internal scattering are characterized by higher optical density than their compact counterparts and high chemical reactivity thanks to extended interfaces with the electrolytic solution. On the other hand one dimensional morphologies – like nanotubes,[21–24] nanowires[21,25,26] and nanorods[27–29] – exhibit enhanced charge transport properties, as the dimensional confinement of their structures results in direct charge diffusion pathways with reduced resistance. Highly crystalline structures[30,31] can further enhance this effect by reducing the density of grain boundaries and defects which constitute charge recombination sites.

Thanks to its band-gap of approximately 2.6 eV, the favorable alignment of its energy levels[4] and a good chemical stability in acidic environment, tungsten trioxide (WO_3) is one of the transition metal oxides currently object of numerous studies. The theoretical performance limits of WO_3, estimated based on its band-gap, are respectively 5 mA/cm^2 for the photocurrent and 6% for the solar-to-hydrogen (STH) efficiency.[32] Photoanodes made by WO_3 nanoparticles[33,34] have been thoroughly studied and optimized, reaching photocurrents up to the range of 2.5 mA/cm^2 with layers as thin as 2.5 μm.[35] Although well performing, nanoparticle films require a high applied bias to efficiently operate, due to the high number of grain boundaries that limit charge transport and enhance charge trapping;[36] the rather high density of the material also hinders its eventual use as a scaffold for subsequent sensitization processes. One dimensional morphologies,[26,37,38] despite the

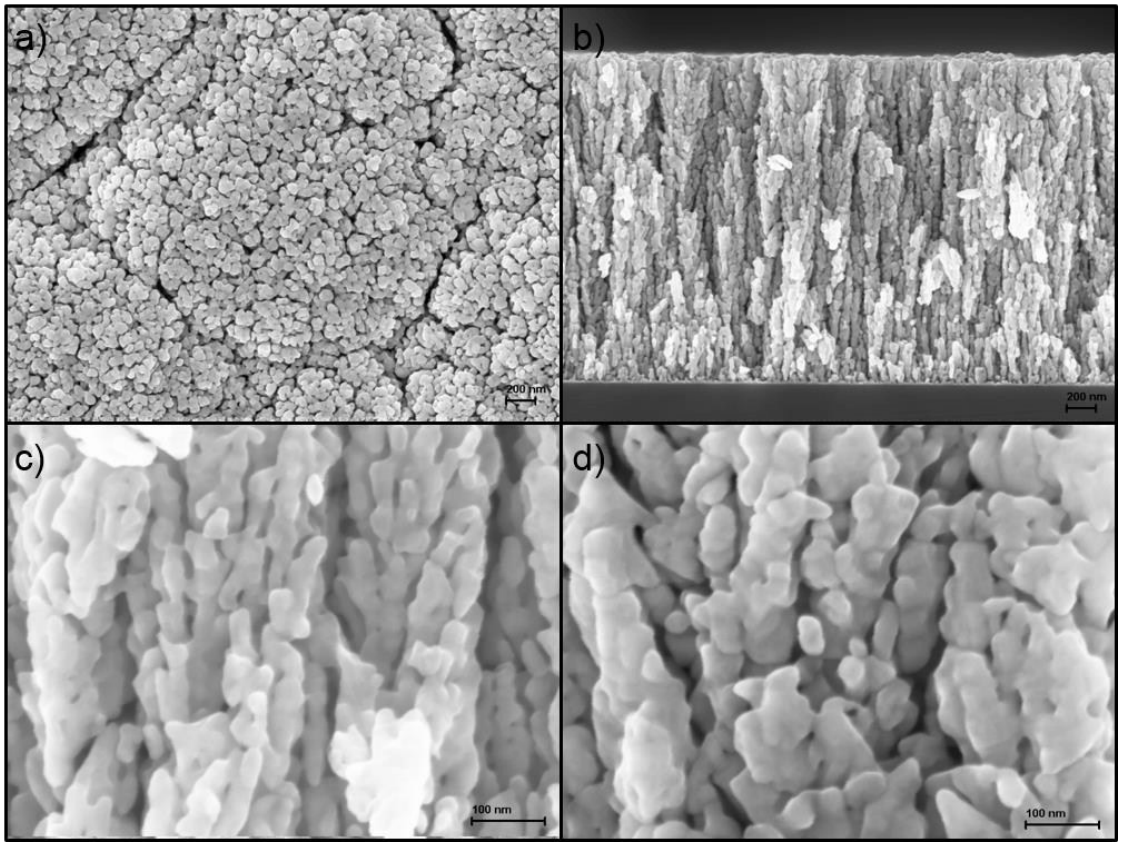

Figure 1. SEM images of the top (a) and cross-sectional (b) view of the nano-tree morphology. SEM images at high magnification of cross-sectional view for both the HYP (c) and HIE (d) samples.

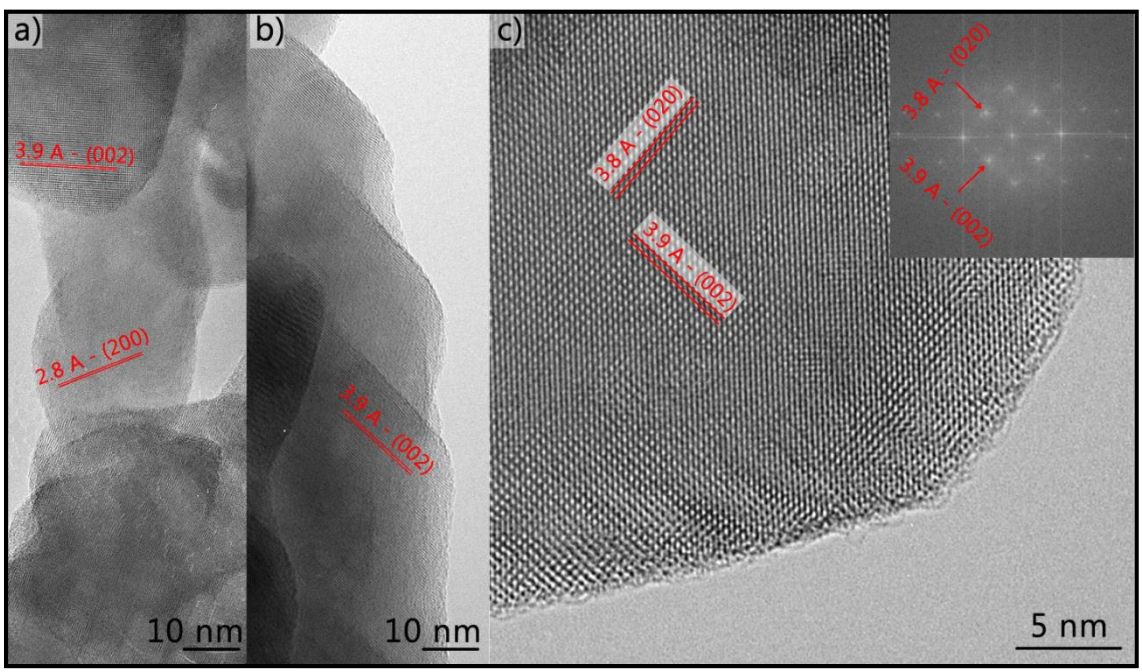

Figure 2. High resolution TEM images of the HIE (a) and HYP (b, c) samples. The HYP sample, here imaged from the [100] zone axis, shows high crystalline quality and clean surface terminations (c). The inset show the Fast Fourier Transform of the lattice, where the main spacings are highlighted.

improved charge transport properties, usually lack the surface area and optical density values required to obtain high photocurrents.

The concept behind this work is to develop a WO_3 photoanode that combines the convenient properties of nanoparticle films with those of 1D morphologies: high volumetric surface area and long range crystalline order with enhanced charge transport

properties. To achieve such concept, hierarchical hyperbranched nano-trees have been developed exploiting gas phase self-assembly using the pulsed laser deposition (PLD) technique.[30,39] As an internal benchmark, non-hyperbranched yet still hierarchical samples have been produced with PLD, showing an onset potential similar to state-of-the-art WO_3 devices present in literature. The thorough comparison between these two closely-related materials allows to draw some general conclusion on the relevance of facet selection and trap density in photoelectrochemical water splitting systems.

Results and discussion

As for previous works that employed the PLD setup to deposit transition metal oxides[30,39–41], the operational parameters of the deposition are here optimized to obtain hierarchical WO_3 nanostructures. In order to show the inherent benefits of a hyperbranched structure in comparison to a less ordered crystalline configuration, two different types of samples fabricated by PLD are used throughout this work: hierarchical hyperbranched WO_3 nanostructures (HYP) and hierarchical WO_3 nanostructures lacking the long range crystalline order (HIE).

SEM images (Figure 1a and 1b) show the distinctive tree-shaped growth shared by both type of sample, comprising a main stem perpendicular to the sample surface from which numerous branches develop, themselves having their own ramifications. This complex hierarchical structure is defined within a conical envelope forming an angle of 15–20° with the main growth axis. At higher magnification (Figure 1c and 1d) it is possible to clearly distinguish the two nanostructure with the HYP more ordered than the HIE.

TEM images (Figure 2a and 2b) show branches developing preferentially towards the *b* direction of the primitive cell and with a lattice spacing that matches the WO_3 (monoclinic α-phase) structure. In the HYP sample, lattice fringes indicate crystalline domains sharing planes along the [001] direction, resulting in larger aggregates with fewer defects. The high degree of crystallinity results in faceted, clean surfaces (Figure 2c).

The preferential growth along the [020] direction is confirmed by XRD spectra (Figure 3), where both the HYP and the HIE samples show a high intensity of the (020) diffraction peak in comparison to the reference powder (labelled as REF). The relative peak height, normalized by the intensity of the adjacent (200) peak, is 1.9 times the reference powder value for the HIE sample and 3.4 times the reference powder value for the HYP one.

The light absorption properties of the film are studied through the absorptance (100-T-R) spectra, measured for both morphologies on the 20-μm-thick samples (Figure 4a). Since the optical measurements are performed by shining light on the glass side of the devices, the contribution of the WO_3 film alone is obtained by subtracting the spectrum of a clean glass plus

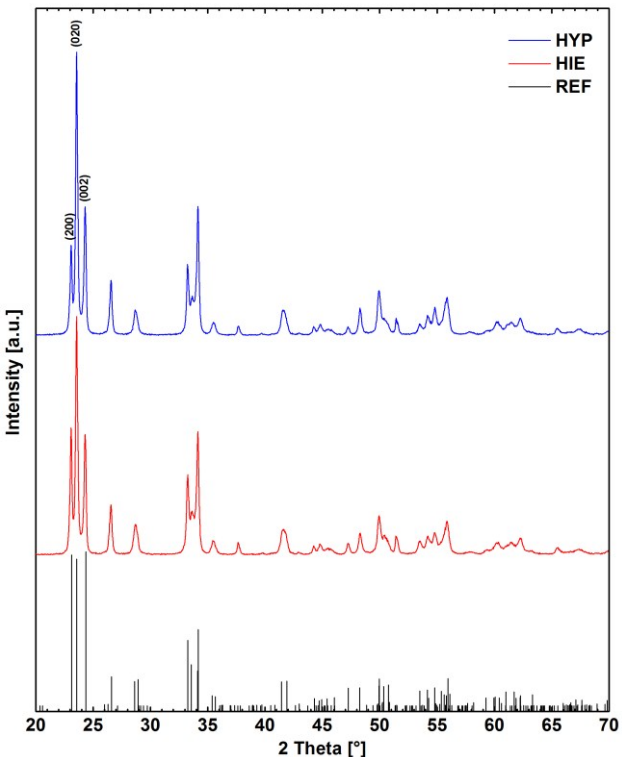

Figure 3. XRD spectra of the HYP and HIE samples, together with the reference peaks WO_3 monoclinic phase represented by REF.

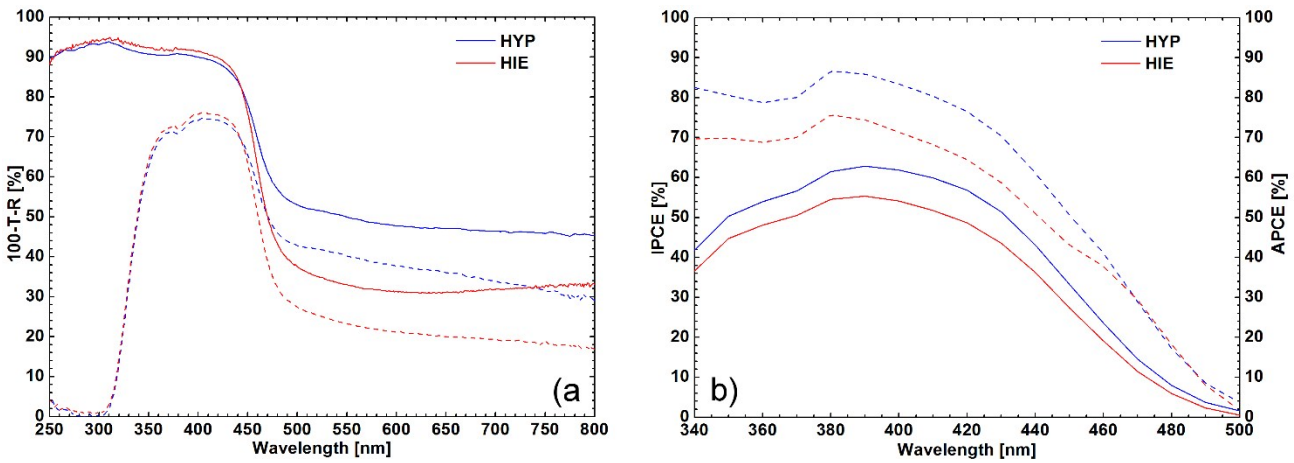

Figure 4. Absorptance spectra (a) of the HYP and HIE 20-μm-thick samples, with the contribution of glass plus FTO (dashed) and without (solid). IPCE (b, solid) and APCE (b, dashed) spectra of the HYP and HIE 20-μm-thick samples, measured by shining light from the glass side and with an applied bias of 1 V vs RHE.

FTO from the experimental data. For photons with energies above the optical band-gap of WO_3 (λ < 470 nm) the integrated light absorption gradually increases and reaches a maximum value around 90% for the WO_3 film on glass plus FTO and around 70% for the WO_3 film only. A significant tail towards the infrared range (λ > 470 nm) is observed for all samples – its intensity increasing with film thickness – and it is attributed to several factors. The constant portion of this contribution comes from the bare glass plus FTO substrate: light with high scattering angles is reflected back or exits through the glass side and it is thus lost during the measurement. The portion that scales with film thickness is related to the scattering properties of the WO_3 nanostructures, useful to increase the light path length through the device and thus the overall absorption of the device. However, the secondary effect of this optical feature is to enhance the back and lateral scattering, resulting in light lost during the measurement that is related to the amount of scattering material present in the film.

Linear sweep voltammetry (LSV) curves are here shown for both the HYP and HIE morphologies deposited with PLD as a function of film thickness (Figure 5). Saturation photocurrent increases with film thickness for both the HYP and HIE morphology. The HIE samples reach saturation with the 20-µm film, with a photocurrent value of 1.77 mA/cm2 at 1.3 V. The HYP samples instead reach saturation already with the 10-µm film, with a value of 1.85 mA/cm^2 at 0.8 V, and further improve the performances with the 20-µm film, showing higher photocurrent values in the voltage range below saturation. Although the saturation photocurrents between the two batches are similar, the photocurrent onset potential and the whole photocurrent slope profile experience a consistent shift between 100-150 mV towards higher voltages, as the nanostructure loses its hyperbranched morphology, with the HYP samples showing an onset voltage of 0.4 V and the HIE samples of 0.5 V. Moreover, the photocurrent exhibited at low biases by the HYP morphology is stable for an extended period of time as shown by chronoamperometry (see Figure S3).

The efficient charge generation and charge injection of the hyperbranched nanostructures can be appreciated from the IPCE spectra (with light shining from the glass side and an applied potential of 1 V versus RHE) performed on the 20-µm-thick samples, together with the calculated APCE spectra (Figure 4b). The IPCE profile shows an onset at approximately 500 nm and a peak value around 400 nm, with a maximum IPCE of 56% for the HIE sample and 63% for the HYP sample. The trend of the IPCE spectra with sample thickness (Figure S2) shows a gradual increase of the curve steepness near the absorption band-edge. This behavior reflects how thicker samples are capable of saturating light absorption thanks to enhanced light scattering properties and thus achieve higher values of internal conversion efficiency close to the band-edge, without losing their performance due to transport-related issues. For nanoparticle films thick samples usually have higher values of light absorption thanks to the increased optical density of the film, but suffer from transport-related issues, as the charges photogenerated deep within the material have higher chances to recombine over the long distances. Quasi-1D morphologies deposited by PLD are capable to overcome this limitation by decoupling charge diffusion from light absorption. While photogenerated electrons travel through the whole nano-tree height, holes can diffuse perpendicularly to the nano-branch axis to reach its surface and be injected in the electrolyte. This is a crucial point since hole diffusion length for monoclinic WO_3 has been estimated to be around 150 nanometers:[32,42] hole

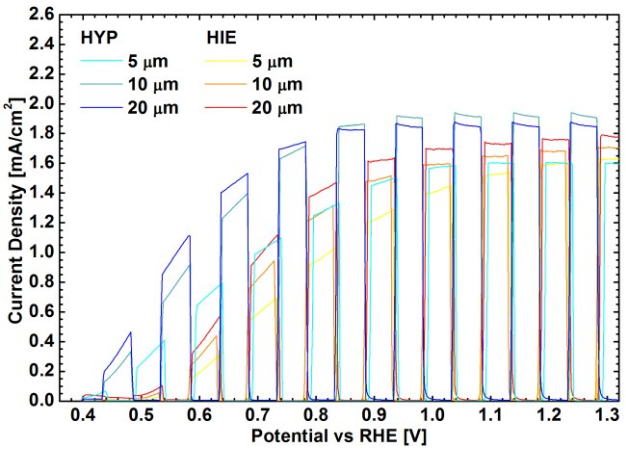

Figure 5. LSV curves of the HYP and HIE samples as a function of film thickness, performed under chopped light in an aqueous solution of 1 M sulfuric acid (H_2SO_4).

diffusion paths in the film are shorter than that value – leading to efficient hole injection – and are independent from film thickness, as they are related to the average crystallite size. Electron diffusion pathways are instead along the nano-brances axis and toward the FTO contact, with an average distance related to the depth at which charge photogeneration occurs. Incident light shined on the glass substrate is firstly absorbed by the "roots" of the nano-trees, thus photogenerating a consistent amount of charges in the spatial region within the first few micrometer of the film, very close to the film/FTO interface. In this way the optical density can be enhanced by increasing the film thickness up to saturation, without lengthening the diffusion pathways of the electrons photogenerated in the first spatial region and thus allowing to increase the internal conversion efficiency without any transport-related issue.

Transport properties, recombination properties and charge accumulation properties of the material are extracted from the electrochemical impedance spectroscopy (EIS) spectra (see Figure S4) and plotted as a function of thickness for the two different morphologies (Figure 6). The electrochemical parameters – and the physical meaning they carry – employed to simulate the working device via the equivalent electric circuit approach (see Figure S5) are taken from previous works of Bisquert group on mesoporous transition metal oxide photoanodes in aqueous electrolyte.[43–45] Charge recombination resistance R_{rec} describes the charge transfer kinetics of electrons recombining with the surface states/species in the solution. HYP samples show higher values of charge recombination resistance than their HIE counterparts as the increased crystalline size and improved long-range order reduce the number of film/solution interfaces and increases the path length for transversal electron diffusion (Figure 6a). Charge recombination resistance for both morphologies is almost constant with thickness as the crystallinity of each configuration is not influenced by the film thickness. Chemical capacitance C_μ is related to the distribution of trap states below the conduction band. From the experimental measurements (Figure 6b), chemical capacitance follows a linear trend with sample thickness for both morphologies, with the HIE samples displaying a higher slope than the HYP samples. The increased chemical capacitance in the HIE samples is attributed to the higher density of traps states due to a more defective crystal lattice of the nano-tree branches. Electron lifetime τ_n is

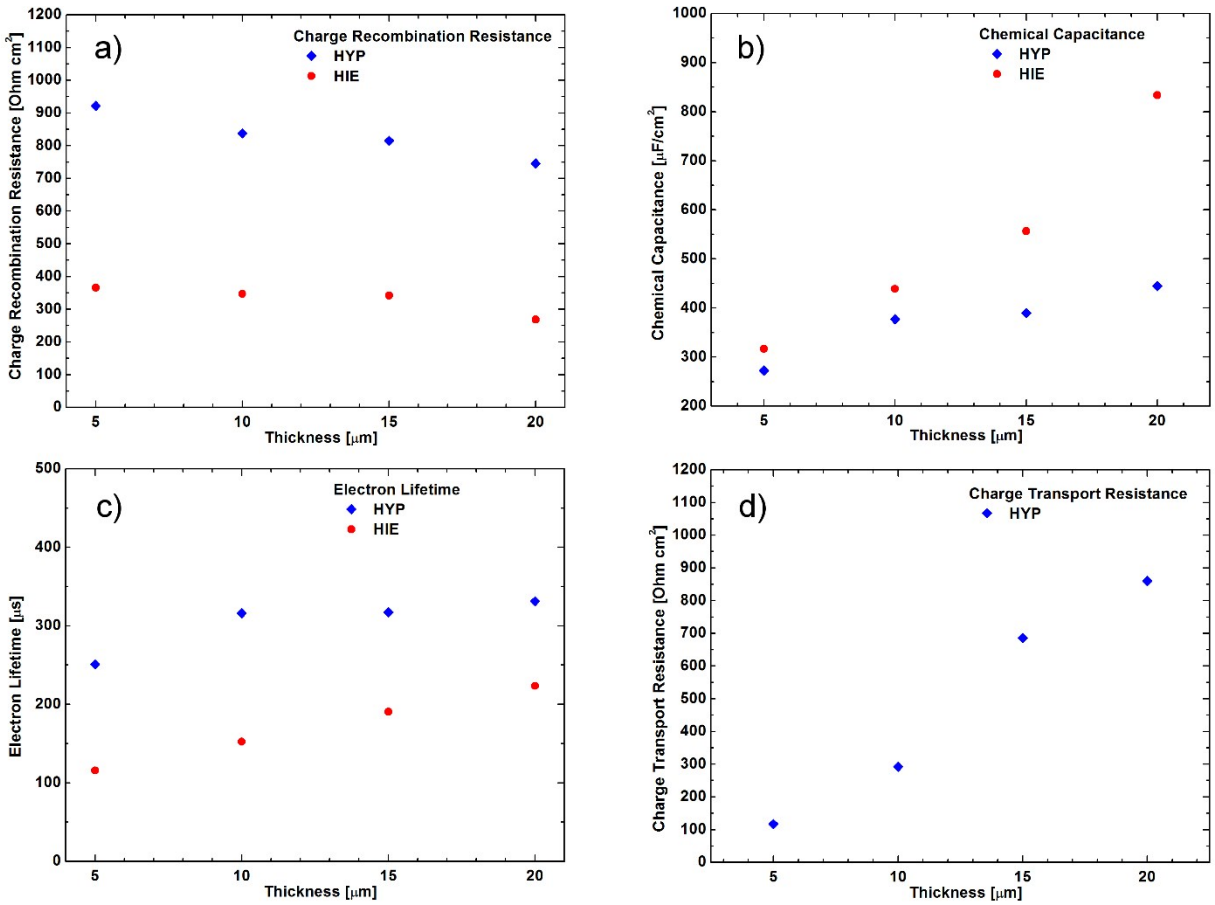

Figure 6. Electrochemical parameters extracted from EIS measurements as a function of thickness for the two different morphologies: charge recombination resistance (a), chemical capacitance (b) and electron lifetime (c). Charge transport resistance (d) is shown for the HYP samples only.

calculated as the product of charge recombination resistance and chemical capacitance.[46] The persistence of photogenerated electrons in the conduction band is related to two different processes: the trapping-detrapping events that delay electrons movement and prolong their presence in the conduction band (related to chemical capacitance C_μ) and the electrons transfer towards recombination centers at the electrolyte interface (related to charge recombination resistance R_{rec}).

$$\tau_n = C_\mu \cdot R_{rec}$$

As the product of two experimental parameters with opposing effect on the overall charge transport, the calculated values of electron lifetime τ_n (Figure 6c) can be somehow misleading without the correct premises. A high charge recombination resistance is desirable as it reduces the chances of the electron travelling towards recombination centers, leading to an actual increase in the electron lifetime in the conduction band. On the other hand a high chemical capacitance means more defect states where electron trapping-detrapping events can occur. Although this effect prolongs the electron lifetime in the conduction band, it happens through delayed processes and thus hinders the electron transport in the structure. Charge transport resistance R_{tr} (Figure 6d) represents the resistance of the whole nanostructured film and – as expected in first approximation – it increases with film thickness. It was possible to extrapolate this parameter only for the HYP samples due to the presence of artifacts in the high frequency region of the Nyquist plot of the HIE samples (see Figure S4). Electron diffusion length L_n for the hyperbranched morphology is hence calculated from the two resistance parameters and the film thickness L.[47,48] The value – constant with thickness since it is a property of the morphology itself – is around 17 μm, in good agreement with the trend shown in the LSV plots by the photocurrent (see Figure 4), that starts saturating for similar values of film thickness.

$$L_n = L \cdot \sqrt{\frac{R_{rec}}{R_{tr}}}$$

Morphologies with a lower crystalline order need higher applied voltages to efficiently extract electrons due to the increased amount of grain boundaries with high defectiveness and thus a higher applied bias is required to start oxidizing water. A possible synergistic mechanism contributing to this behavior could be that directional growth along the *b* crystalline axis forces the photo-oxidation of water to take place mainly at the [200] and [002] crystalline surfaces, where the evolution over-potential has been calculated to be 50-60 mV lower that the over-potential shown by the [020] surface.[49]

Conclusions

In summary, quasi-1D WO_3 nanostructures are deposited by PLD and by tuning the deposition parameters, hyperbranching and long range crystalline order is achieved. Both hierarchical tree-like structures present efficient light absorption and internal scattering with enhanced charge collection efficiency

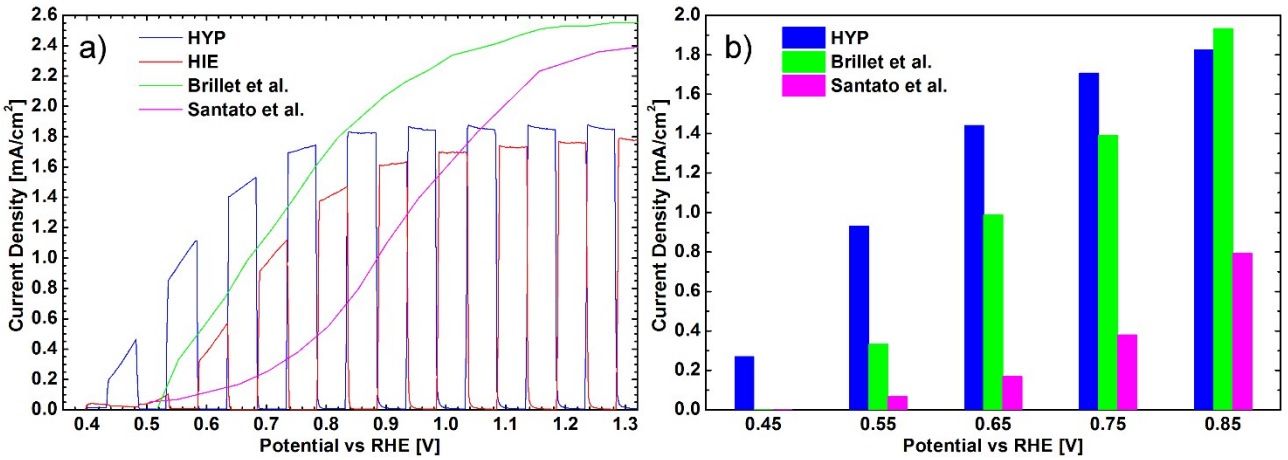

Figure 7. LSV curves (a) of the HYP and HIE 20-µm-thick samples performed under chopped light in an aqueous solution of 1 M sulfuric acid (H_2SO_4), the 2.5-µm-thick sample from Brillet et al.[35] and 2-µm-thick sample from Santato et al.[50] performed under continuous light in a 1 M perchloric acid ($HClO_4$). Histogram comparison (b) of the photocurrent values at different applied voltages.

despite the large thickness thanks to the mesoporous structure of the film. The difference between the two configurations becomes evident in the electrochemical results: both morphologies present a photocurrent saturation value around 1.8 mA/cm^2, but the onset voltage of the hyperbranched samples is 0.4 V versus RHE, approximately 100-150 mV lower than the samples without hyperbranching. The whole photocurrent trend is shifted towards a lower potential and the slope of the curve is increased for the hyperbranched samples, reaching saturation at an early value of 0.8 V versus RHE.

A comparison with state-of-the-art photoanodes taken from the literature[35,50] (Figure 7a and 7b) show that, despite a lower photocurrent, hyperbranched samples deposited by PLD exhibit a major advantage in the low bias region thanks to their reduced photocurrent onset potential. On the other hand, the hierarchical samples present a photocurrent onset and slope similar to that of nanoparticle films taken from literature. These improved performances are attributed to the long-range crystalline order of the hyperbranched morphology – with directional growth three times more pronounced than the reference monoclinic WO_3 and crystallites in the order of 100 nm – which results in enhanced charge injection and charge transport properties. Longer crystals yield less grain boundaries where charge recombination can occur and the elongated directional growth of the branches favors the transport of the electron towards the FTO contact along the tree axis. Moreover, the preferential exposure of the [200] and [002] crystalline surfaces is believed to lower the overpotential for water oxidation. Quasi-1D hyperbranched WO_3 nanostructures represent a promising morphology for the realization of water-splitting photoanodes and hold a promise for future doping or sensitization experiments thanks to their high surface area and directional porous structure. Despite the saturation photocurrent values are lower than the best performing devices present in literature, the low onset potential and high curve steepness represent an unprecedented case for water-splitting photoanodes that allow to achieve high values of photocurrent at low applied bias.

Experimental section

Film growth

The tungsten trioxide nanostructures are deposited via PLD, ablating a tungsten trioxide target with laser pulses from a KrF excimer laser (wavelength 248 nm, repetition rate 20 Hz) within a vacuum chamber (base vacuum in the order of 10^{-3} Pa) filled with O_2 background gas up to the desired working pressure. Briefly, in PLD a laser pulse impinges on the target that is locally vaporized and partially ionized, generating a plasma that expands supersonically towards the substrate. The ablated species condense on the substrate, forming a film the properties of which can be controlled by varying background gas pressure, laser fluence and target to substrate distance. In a certain processing window, typical for each material, it is possible to induce gas-phase nucleation of clusters, which are then scattered upon interaction with the background gas, causing self-assembly of arrays of quasi-1D nanostructures, with a typical diameter of hundreds of nanometers and heights linear with the deposition time.[30]

Quasi 1D hyperbranched and hierarchical WO3 photoanodes are grown on 2.3-mm-thick soda-lime glasses slides coated with a FTO conductive coating (sheet resistance of 15 Ω/sq). All samples are deposited at room temperature, yielding amorphous films. The crystalline phase transition is achieved through a post-deposition annealing treatment, performed in a muffle furnace in air for 2 hours at 500°C. Similarly to the previously reported hyperbranched TiO_2,[30] different background pressures yield WO_3 films ranging from compact to extremely porous, with a small operational window where hyperbranched nanostructures are obtained. The range for hierarchical structures is found between 10 Pa and 60 Pa (with a target to substrate distance of 5 cm and a laser fluence of 3.4 J/cm^2), with an optimum value to obtain hyperbranching of 20 Pa oxygen of background pressure with a film growth rate of 2.4 nm/s. Out of this window, for example increasing laser fluence and keeping all other parameters constant, morphologies that still display the characteristic tree-shape hierarchical structure, but lose the hyperbranched nature are obtained. This control on the morphology and structure of the films is exploited to obtain the hyperbranched (HYP) and hierarchical (HIE) photoanodes discussed in this work.

Characterization

Film morphology is investigated using a Field Emission Scanning Electron Microscope (Zeiss SUPRA 40) and a High Resolution Transmission Electron Microscope (JEOL 4000EX

with LaB_6 filament operated at 400kV accelerating voltage). Additional information on the crystallinity of the films is obtained through X-ray diffraction (Philips X'Pert, Cu K_α radiation, Hanawalt phase identification method on PDF-2 dataset).

The optical properties of the samples are measured with a UV/VIS/NIR spectrometer (Perkin Elmer Lambda 1050) operating with an integrating sphere. The absorptance is calculated from the experimental transmittance and reflectance data with the following formula:

$$A = 100 - T - R$$

where A is the absorptance, T is the transmittance and R is the reflectance.

LSV measurements are carried out using a potentiostat/galvanostat (Autolab PGSTAT 30) with a scan rate of 20 mV/s in a 3-electrodes configuration, with a WO_3 sample as the working electrode, a platinum wire (surface area of 0.8 mm^2) as the counter electrode and Ag/AgCl in saturated KCl as the reference electrode; the electrolyte is an aqueous solution of 1M H_2SO_4 with a pH of 0; illumination is provided by a Class AAA solar simulator (Oriel Model 94063A) that simulates the AM 1.5G solar spectrum with an average intensity of 100 mW/cm^2.

EIS measurements employ the same setup as LSV and are performed by applying a 20 mV amplitude perturbation between 10,000 Hz and 0.01 Hz at a voltage of 0.7 V versus RHE. The applied bias chosen for the EIS measurements is the potential of maximum power output for the devices realized with HYP samples (see Figure S1).

Incident Photon to Current Efficiency (IPCE) spectra are obtained using the same 3-electrodes configuration described above, with a 150 W Xenon lamp coupled with a monochromator (Applied Photophysics, 1200 lines/mm, band-pass 10 nm). The bias potential is applied with a potentiostat (AMEL model 552), the photocurrent signal is recorded with a multimeter (Agilent 34401A, 61/2 digits) and the incident irradiance is measured with a calibrated silicon photodiode (Centronic OSD 7Q). The final IPCE values are calculated from the experimental data according to the following formula:

$$IPCE = 1.24 \times 10^3 \times \frac{J\left(\frac{\mu A}{cm^2}\right)}{\lambda(nm) \times P\left(\frac{W}{cm^2}\right)}$$

where J is the photocurrent density, λ is the wavelength of the incident light and P is the radiant power density at that given wavelength. Absorbed Photon to Current Efficiency (APCE) spectra are hence calculated using the following relation:

$$APCE = \frac{IPCE}{A}$$

where A is the actual absorptance of the mesoporous film, obtained by subtracting the absorptance of the bare glass plus FTO form the absorptance of the whole sample.

Acknowledgements

M.B. and A.M. and F.D.F acknowledge financial support from European Union through projects PHOCS, ENERGY 2012-10.2.1, Future Emerging Technologies Collaborative Project, grant N. 309223.

G.D. and C.D. acknowledge funding from the ERC under grant number 259619 PHOTO EM.

Notes and references

[a] Center for Nano Science and Technology@PoliMI, Istituto Italiano di Tecnologia, Via Giovanni Pascoli 70/3, 20133 Milano, Italy

[b] Dipartimento di Energia, Politecnico di Milano, Via Ponzio 34/3, 20133 Milano, Italy

[c] Dipartimento di Fisica, Politecnico di Milano, Piazza Leonardo da Vinci 32, 20133 Milano, Italy

[d] Eni S.p.A., Istituto ENI Donegani, Via Giacomo Fauser 4, 28100 Novara, Italy

[e] Department of Materials Science & Metallurgy, University of Cambridge, 27 Charles Babbage Road, CB3 0FS, Cambridge, United Kingdom

† M.B. and A.M. contributed equally.

Electronic Supplementary Information (ESI) available: Full experimental work concerning the thickness analysis of the samples performed through power efficiency curves, IPCE curves and Nyquist impedance plots. See DOI: 10.1039/b000000x/

1. A. Fujishima and K. Honda, *Nature*, 1972, **238**, 37–38.
2. A. Kudo and Y. Miseki, *Chem. Soc. Rev.*, 2009, **38**, 253–78.
3. L. Meda and L. Abbondanza, *Rev. Adv. Sci. Eng.*, 2013, **2**, 200–207.
4. M. Grätzel, *Nature*, 2001, **414**.
5. Z. Li, W. Luo, M. Zhang, J. Feng and Z. Zou, *Energy Environ. Sci.*, 2013, **6**, 347.
6. J. H. Park, S. Kim and A. J. Bard, *Nano Lett.*, 2006, **6**, 24–8.
7. K. Palanivelu, J. S. Im and Y. Lee, *Korean Carbon Soc.*, 2007, **8**, 214–224.
8. C. Di Valentin, G. Pacchioni and A. Selloni, *Chem. Mater.*, 2005, 6656–6665.
9. D. Wang, J. Tang, J. Ye and Z. Zou, *Mater. Sci. Forum*, 2003, **423-425**, 163–166.
10. F. Wang, C. Di Valentin and G. Pacchioni, *J. Phys. Chem. C*, 2012.
11. C. Yang, Z. Wang, T. Lin, H. Yin, X. Lü, D. Wan, T. Xu, C. Zheng, J. Lin, F. Huang, X. Xie and M. Jiang, *J. Am. Chem. Soc.*, 2013, **135**, 17831–8.
12. S. Tilley, M. Cornuz, K. Sivula and M. Grätzel, *Angew. Chemie*, 2010, **49**, 6405–8.
13. S. Linic, P. Christopher and D. Ingram, *Nat. Mater.*, 2011, **10**, 911–21.
14. F. Di Fonzo, A. Bailini, V. Russo, A. Baserga, D. Cattaneo, M. G. Beghi, P. M. Ossi, C. S. Casari, A. Li Bassi and C. E. Bottani, *Catal. Today*, 2006, **116**, 69–73.
15. W. Kim, T. Tachikawa, D. Monllor-Satoca, H. Kim, T. Majima and W. Choi, *Energy Environ. Sci.*, 2013, **6**, 3732.

16. L. Teoh, J. Shieh, W. Lai, I. Hung and M. Hon, *J. Alloys Compd.*, 2005, **396**, 251–254.

17. K. Sivula, R. Zboril, F. Le Formal, R. Robert, A. Weidenkaff, J. Tucek, J. Frydrych and M. Grätzel, *J. Am. Chem. Soc.*, 2010, **132**, 7436–44.

18. S. Y. Ryu, W. Balcerski, T. K. Lee and M. R. Hoffmann, *J. Phys. Chem. C*, 2007, **111**, 18195–18203.

19. a. Królikowska, P. Barczuk, R. Jurczakowski and J. Augustynski, *J. Electroanal. Chem.*, 2011, **662**, 229–239.

20. J. K. Kim, K. Shin, S. M. Cho, T.-W. Lee and J. H. Park, *Energy Environ. Sci.*, 2011, **4**, 1465.

21. P. M. Rao, I. S. Cho and X. Zheng, *Proc. Combust. Inst.*, 2013, **34**, 2187–2195.

22. S. Bai, H. Li, Y. Guan and S. Jiang, *Appl. Surf. Sci.*, 2011, **257**, 6406–6409.

23. Z. Zhang, M. F. Hossain and T. Takahashi, *Int. J. Hydrogen Energy*, 2010, **35**, 8528–8535.

24. J. Park, S. Kim and A. Bard, *Nano Lett.*, 2006, **6**, 24–8.

25. X. Feng, K. Shankar, O. K. Varghese, M. Paulose, T. J. Latempa and C. a Grimes, *Nano Lett.*, 2008, **8**, 3781–6.

26. J. Su, X. Feng, J. D. Sloppy, L. Guo and C. a Grimes, *Nano Lett.*, 2011, **11**, 203–8.

27. I. S. Cho, Z. Chen, A. J. Forman, D. R. Kim, P. M. Rao, T. F. Jaramillo and X. Zheng, *Nano Lett.*, 2011, **11**, 4978–84.

28. Z. G. Yu, C. E. Pryor, W. H. Lau, M. a Berding and D. B. MacQueen, *J. Phys. Chem. B*, 2005, **109**, 22913–9.

29. J. H. Bang and P. V. Kamat, *Adv. Funct. Mater.*, 2010, **20**, 1970–1976.

30. L. Passoni, F. Ghods and P. Docampo, *ACS Nano*, 2013, 10023–10031.

31. R. Buonsanti and E. Carlino, *J. Am. Chem. Soc.*, 2011, **133**, 19216–39.

32. C. A. Bignozzi, S. Caramori, V. Cristino, R. Argazzi, L. Meda and A. Tacca, *Chem. Soc. Rev.*, 2013, **42**, 2228–46.

33. R. Solarska, R. Jurczakowski and J. Augustynski, *Nanoscale*, 2012, **4**, 1553–6.

34. Y. Guo, X. Quan and N. Lu, *Environ. Sci. Technol.*, 2007, **41**, 4422–7.

35. J. Brillet, J.-H. Yum, M. Cornuz, T. Hisatomi, R. Solarska, J. Augustynski, M. Graetzel and K. Sivula, *Nat. Photonics*, 2012, **6**, 824–828.

36. G. R. Bamwenda and H. Arakawa, *Appl. Catal. A Gen.*, 2001, **210**, 181–191.

37. P. M. Rao, L. Cai, C. Liu, I. S. Cho, C. H. Lee, J. M. Weisse, P. Yang and X. Zheng, *Nano Lett.*, 2014, **14**, 1099–105.

38. S. K. Pilli, R. Janarthanan, T. G. Deutsch, T. E. Furtak, L. D. Brown, J. a Turner and A. M. Herring, *Phys. Chem. Chem. Phys.*, 2013, **15**, 14723–8.

39. F. Sauvage, F. Di Fonzo, a Li Bassi, C. S. Casari, V. Russo, G. Divitini, C. Ducati, C. E. Bottani, P. Comte and M. Graetzel, *Nano Lett.*, 2010, **10**, 2562–7.

40. F. Di Fonzo, C. S. Casari, V. Russo, M. F. Brunella, A. Li Bassi and C. E. Bottani, *Nanotechnology*, 2009, **20**, 015604.

41. F. Di Fonzo, D. Tonini, A. Li Bassi, C. S. Casari, M. G. Beghi, C. E. Bottani, D. Gastaldi, P. Vena and R. Contro, *Appl. Phys. A*, 2008, **93**, 765–769.

42. M. Butler, *J. Appl. Phys.*, 1977, **48**, 1914.

43. S. Gimenez, H. K. Dunn, P. Rodenas, F. Fabregat-Santiago, S. G. Miralles, E. M. Barea, R. Trevisan, A. Guerrero and J. Bisquert, *J. Electroanal. Chem.*, 2012, **668**, 119–125.

44. J. Bisquert, G. Garcia-Belmonte, F. Fabregat-Santiago, N. S. Ferriols, P. Bogdanoff and E. C. Pereira, *J. Phys. Chem. B*, 2000, **104**, 2287–2298.

45. J. Bisquert, *Phys. Chem. Chem. Phys.*, 2003, **5**, 5360.

46. J. Bisquert, F. Fabregat-Santiago, I. Mora-Seró, G. Garcia-Belmonte and S. Giménez, *J. Phys. Chem. C*, 2009, **113**, 17278–17290.

47. J. Bisquert and I. Mora-Seró, *J. Phys. Chem. Lett.*, 2010, **1**, 450–456.

48. J. Bisquert, *J. Phys. Chem. B*, 2002, **106**, 325–333.

49. A. Valdés and G.-J. Kroes, *J. Chem. Phys.*, 2009, **130**, 114701.

50. C. Santato, M. Ulmann and J. Augustynski, *J. Phys. Chem. B*, 2001, **105**, 936–940.

